Atmos. Chem. Phys. Discuss., 11, 8385–8430, 2011
www.atmos-chem-phys-discuss.net/11/8385/2011/
doi:10.5194/acpd-11-8385-2011

Atmospheric Chemistry and Physics Discussions

Simulating deep convection with a shallow convection scheme

C. Hohenegger and C. S. Bretherton

Department of Atmospheric Sciences, University of Washington, Seattle, WA, USA

Received: 10 December 2010 – Accepted: 28 February 2011 – Published: 11 March 2011

Correspondence to: C. Hohenegger (cathy.hohenegger@zmaw.de)

Published by Copernicus Publications on behalf of the European Geosciences Union.

Abstract

Convective processes profoundly affect the global water and energy balance of our planet but remain a challenge for global climate modeling. Here we develop and investigate the suitability of a unified convection scheme, capable of handling both shallow and deep convection, to simulate cases of tropical oceanic convection, mid-latitude continental convection, and maritime shallow convection. To that aim, we employ large-eddy simulations (LES) as a benchmark to test and refine a unified convection scheme implemented in the Single-Column Community Atmosphere Model (SCAM). Our approach is motivated by previous cloud-resolving modeling studies, which have documented the gradual transition between shallow and deep convection and its possible importance for the simulated precipitation diurnal cycle.

Analysis of the LES reveals that differences between shallow and deep convection, regarding cloud-base properties as well as entrainment/detrainment rates, can be related to the evaporation of precipitation. Parameterizing such effects and accordingly modifying the University of Washington shallow convection scheme, it is found that the new unified scheme can represent both shallow and deep convection as well as tropical and continental convection. Compared to the default SCAM version, the new scheme especially improves relative humidity, cloud cover and mass flux profiles. The new unified scheme also removes the well-known too early onset and peak of convective precipitation over mid-latitude continental areas.

1 Introduction

Accurate representation of deep convection with global climate models of coarse resolution remains a nagging problem for the simulation of present-day and future climates. Typical biases include the simulation of a double Inter-Tropical Convergence Zone (ITCZ, see e.g., Bretherton, 2007; Lin, 2007), a too weak, too fast or spatially distorted Madden-Julian Oscillation (MJO, see e.g., Slingo et al., 1996; Bretherton, 2007)

ACPD
11, 8385–8430, 2011

and poor timing of convection with a too early onset, peak and decay of precipitation. This last bias is apparent both over the Tropics (e.g., Yang and Slingo, 2001; Bechtold et al., 2004) and mid-latitude continental areas (e.g., Dai et al., 1999; Lee et al., 2007).

Many approaches have been proposed over the years to parameterize deep convection (see e.g., Arakawa, 2004; Randall et al., 2003, for a review). The most popular method remains the use of a mass flux scheme (see e.g., Plant, 2010; Arakawa and Schubert, 1974). The latter aims to predict the vertical structure and evolution of a one-dimensional entraining-detraining plume (bulk mass flux scheme) or spectrum thereof (spectral mass flux scheme). Irrespective of the specific design, convection schemes have to rely on some assumptions to relate the sub-scale cloud behavior to the large-scale resolved flow. Such relations are hard to get from observations and hard to formulate.

Recently, the use of large-eddy or cloud-resolving simulations to characterize the behavior of the cumulus ensemble has allowed the formulation of improved convective parameterizations. Rio et al. (2009) were able to simulate a realistic diurnal cycle of convection for an idealized case of mid-latitude continental convection by adding a density current parameterization to Emanuel (1991)'s convection scheme. Grandpeix et al. (2010) investigated this approach for the Hydrology-Atmosphere Pilot Experiment in the Sahel (HAPEX-Sahel) and the Tropical Ocean Global Atmosphere Coupled Ocean Atmosphere Response Experiment (TOGA COARE) and found good agreement with cloud-resolving model simulations. Several studies also documented improvements in tropical convection, without nevertheless being able to fully remove the ITCZ or MJO biases, by employing more elaborate entrainment/detrainment formulations (e.g., Chikira and Sugiyama, 2010; Bechtold et al., 2008; Li et al., 2007; Wang et al., 2007), revised closures/triggering functions (e.g., Deng and Wu, 2010; Li et al., 2007; Zhang and Mu, 2005; Neale et al., 2008) or by introducing convective momentum transport (e.g., Deng and Wu, 2010; Richter and Rasch, 2008). The possible impacts of such modifications are in general strongly model dependent and confined to certain aspects of the simulated convection. In this respect it is still not clear whether a single con-

ACPD
11, 8385–8430, 2011

vective parameterization can realistically handle both tropical oceanic and mid-latitude continental convection.

This study is geared towards improving the simulation of deep convection in coarse-resolution climate models. In contrast to the approach employed in most such models, we seek to develop a unified convection scheme starting from a parameterization designed for shallow cumulus convection. We regard shallow convection as mostly non-precipitating convection with no ice formation. Deep convection will refer to precipitating convection. Cloud-resolving modeling studies have documented the gradual transition occurring from shallow to deep convection and highlighted its importance for the simulated convective diurnal cycle (e.g., Guichard et al., 2004). This may be best achieved with a unified scheme. Our study is a step in this sense. We will explore how to unify shallow and deep convection and present single-column model experiments to test our results.

The basic hypothesis behind our approach is that the main difference between shallow and deep convection is precipitation (both rain and snow) and its effects. Evaporation of precipitation modifies the atmospheric environment and especially the structure of the planetary boundary layer (PBL), which feeds back on the convective development. Including such effects in a shallow convection scheme should thus allow the representation of deep convection within the same scheme. We thus see deep convection as highly interactive with the PBL state, like shallow convection.

In order to fulfill our goals and test our hypothesis, we will employ large-eddy simulations of different convective events. We will investigate modifications in the PBL structure and in the atmospheric environment due to falling precipitation, and derive appropriate relations to describe them. These relations will then be implemented in the shallow convection scheme developed at the University of Washington (UW) by Bretherton et al. (2004) and Park and Bretherton (2009). Using a single-column version of the National Center for Atmospheric Research (NCAR) Community Atmosphere Model (CAM), the performance of the new unified scheme will be assessed against large-eddy simulations, the default version of the CAM single-column model, and a

ACPD
11, 8385–8430, 2011

version of the single-column model in which the UW shallow convection scheme is used without modification (but also without any separate deep convection scheme).

The outline is as follows. Section 2 presents our method with a description of the different models, cases considered, and our experimental set-up. Section 3 focuses on the planetary boundary layer; changes in cloud-base mass flux and cloud-base thermodynamic properties between shallow and deep convection are investigated, parameterized and tested with single-column model experiments. Section 4 repeats the analysis for entrainment and detrainment rates. Conclusions are given in Sect. 5.

2 Method

2.1 Models

The large-eddy simulations (LES) are performed with the System for Atmospheric Modeling (SAM, see Khairoutdinov and Randall, 2003). The model solves the 3D anelastic equations given prescribed large-scale tendencies and surface fluxes/sea surface temperature. As parameterization, the model includes a bulk microphysics scheme, a Smagorinsky-type scheme to represent subgrid-scale turbulence, and the radiation package (Collins et al., 2006) taken from the NCAR CAM3 global climate model (GCM). A more detailed description of SAM can be found in Khairoutdinov and Randall (2003).

For the single-column model experiments we employ the Single-column (one-dimensional) version of the Community Atmosphere Model (SCAM, see Hack and Pedretti, 2000), version 3.5. SCAM comes with the full atmospheric parameterization package of the CAM3.5 GCM. This is a version of CAM3 (see Collins et al., 2006) with a modified treatment of deep convective momentum transport (Richter and Rasch, 2008) and a revised deep convective trigger (Neale et al., 2008). CAM3 includes a surface-driven boundary-layer turbulence scheme based on Holtslag and Boville (1993). Deep convection is parameterized after Zhang and McFarlane (1995) while shallow convection follows Hack (1994). As alternate parameterizations, the model can be run with new

ACPD
11, 8385–8430, 2011

moist turbulence and shallow convection schemes developed at the UW (see Bretherton and Park, 2009; Bretherton et al., 2004; Park and Bretherton, 2009).

2.2 The UW shallow convection scheme

Since the UW shallow convection scheme serves as starting point to develop a unified convection scheme, it is explained here in more detail. It is a mass flux scheme based on a buoyancy-sorting, entrainment-detrainment plume model. The mass flux closure is determined by the ratio between convective inhibition (CIN) and mean planetary boundary layer (PBL) turbulent kinetic energy (TKE).

Cloud properties are expressed in terms of the total water mixing ratio $q_t = q_v + q_l + q_i$ and the ice-liquid water potential temperature $\theta_{li} = \theta - q_l L_v/\Pi c_p - q_i L_f/\Pi c_p$ (Deardorff, 1976), with θ potential temperature, q_i, q_l and q_v the ice, liquid water and water vapor mixing ratios, L_v and L_f the latent heat of vaporization and of sublimation, c_p the specific heat of dry air at constant pressure, and Π the Exner pressure function. Both q_t and θ_{li} are assumed to be conserved for non-precipitating moist adiabatic processes. At cloud base, q_t is set to its surface value, while θ_{li} equates its minimum value over the PBL. Vertical velocity is diagnosed after Eq. (15) of Bretherton et al. (2004) and determines the maximum height reached by the plume.

Entrainment and detrainment processes are parameterized using buoyancy sorting principles. Mixing of cloudy air with environmental air generates a spectrum of mixtures with different buoyancy and vertical velocities. It is assumed that only mixtures that can travel a certain vertical distance remain in the updraft. By assuming that the generated spectrum of mixtures is uniform, the fractional entrainment and detrainment rates per unit height are found to be $\epsilon = \epsilon_0 \chi_c^2$ and $\delta = \epsilon_0 (1-\chi_c)^2$, respectively. The critical mixing fraction χ_c depends on height; at each level it is fully determined by the updraft and environmental properties (see Eq. (B1) in Bretherton et al., 2004). The fractional mixing rate ϵ_0 (m^{-1}) is set empirically to $8/z$, with z (m) being the height above ground. The scheme also includes enhanced penetrative entrainment above the level of neutral buoyancy of the bulk updraft (see Eq. (D1) in Bretherton et al., 2004).

ACPD
11, 8385–8430, 2011

The UW shallow convection scheme employs extremely simple microphysics: condensate larger than $1\,g\,kg^{-1}$ is removed from the updraft as precipitation, which is partitioned between a fixed fraction that can fall through the updraft (and which can only evaporate below the cumulus base) and a remainder that is detrained into the environment (and which can evaporate above cloud base). In either case, the evaporation rate depends upon the saturation deficit and the precipitation flux. Note that while evaporation of precipitation drives organized downdrafts in reality, there is no explicit downdraft formulation in the scheme; evaporated precipitation homogeneously cools the entire grid cell.

In principle, the UW shallow convection scheme could be directly used to predict deep convection. It contains a representation of precipitation and ice formation processes as well as of evaporation. However, it does not include any feedback between falling precipitation and subsequent convective development, which, as stated in the introduction, might be important for deep convection. Within the framework of a bulk mass flux scheme, cloud-base mass flux, cloud-base properties and entrainment/detrainment rates are key quantities controlling the cloud development. Those are thus the three quantities that we will examine in more details in Sects. 3 and 4 and modify with appropriate relationships to design a unified convection scheme.

2.3 Cases

In order to investigate issues related with the parameterization of moist convection, we consider three cases that have been well observed and extensively studied in the past. They have been chosen to span diverse atmospheric conditions and types of convection.

The first case is taken from measurements made at the Atmospheric Radiation Measurement (ARM) Southern Great Plain station between 18 June and 3 July 1997 (Julian days 170–185). This case typifies continental summertime mid-latitude convection. The period encompasses a wide range of conditions, including clear days, shallow convection, diurnally forced convection, and precipitation associated with the passage of

ACPD
11, 8385–8430, 2011

extratropical cyclones and fronts.

The second case represents tropical marine deep convection. The measurements are taken from the Kwajalein Experiment (KWAJEX) over the west Pacific warm pool. We restrict here our analysis to the period 23 July–4 September 1999 (Julian days 204–257).

Finally, we also consider the Barbados Oceanographic and Meteorological Experiment (BOMEX), a frequently simulated example of non-precipitating shallow trade-cumulus convection. The forcing data are derived from observations taken on 22–23 June 1969.

2.4 Experimental set-up

The three cases are simulated with SAM and with different versions of SCAM, using prescribed time-dependent profiles of large-scale vertical motion and horizontal advective heating and moistening as well as surface fluxes (for ARM) and sea surface temperature (for KWAJEX and BOMEX). Each SAM simulation is doubly periodic in the horizontal but employs a different grid. For the ARM case, SAM is run with a horizontal resolution of 500 m with 384×384 grid points and 96 vertical levels going up to 30 km. The grid spacing varies between 50 m near the surface to 250 m in the mid-troposphere. The KWAJEX simulation has a horizontal resolution of 1000 m and a vertical resolution of 100 m near the surface up to 400 m in the mid-troposphere. The domain contains 256×256×64 grid points. For both ARM and KWAJEX, the domain-mean winds are nudged to the time-varying observational profiles with a one-hour relaxation time. Finally, the BOMEX simulation contains 192×192×96 grid points with a resolution (both horizontally and vertically) of 40 m. In the upper third of the domain, perturbations to the horizontal mean are linearly damped to help absorb convectively-forced gravity waves. For BOMEX, the winds are forced by a geostrophic wind profile rather than through nudging.

Similar simulations of SAM have been validated and investigated in detail by Khairoutdinov and Randall (2003) for ARM, Blossey et al. (2007) for KWAJEX, and Siebesma

ACPD
11, 8385–8430, 2011

et al. (2003) for BOMEX. These studies show that the SAM model reproduces the overall convective development fairly accurately compared to observations in all three cases. Hence, we will use the SAM simulations as a benchmark both to characterize the behavior of the cumulus ensemble and to validate the SCAM single-column model experiments.

For all cases, SCAM is run with 30 vertical levels and a time step of 5 min, driven by the same large-scale forcing and surface fluxes/sea surface temperature as SAM. For KWAJEX and BOMEX, the start and end times of the SCAM simulations coincide with the SAM integrations. For ARM, only specific rain events are simulated with SCAM instead of the full time period as a whole. This is to ensure that differences obtained between the integrations are due to the convective parameterization rather than to the simulation of different atmospheric conditions. Indeed, SCAM drifts away from SAM with time in ARM due mainly to different timings and amplitudes of individual rain events. For each rain event, we employ the SAM-simulated mean profiles as initial data for the SCAM simulations. The specific events that we simulate (see, e.g. Fig. 1) are days 174 (05:30 UTC Julian day (JD) 174 to 11:30 UTC JD 175), 176 (05:30 UTC JD 176–11:30 UTC JD 177), 178 (05:30 UTC JD 178–05:30 UTC JD 179), 179 (05:30 UTC JD 179–05:30 UTC JD 180) and 180 (05:30 UTC JD 180–11:30 UTC JD 181). Days with strong large-scale forcing are omitted since SCAM will tend to perform well for those cases due to the use of prescribed large-scale tendencies.

To investigate the performance of the new unified convection scheme, three main types of SCAM simulations are performed (Table 1). The first experiment employs the default version of the CAM3.5 model, in which PBL processes are parameterized after Holtslag and Boville (1993), shallow convection after Hack (1994) and deep convection after Zhang and McFarlane (1995). This simulation is called CAM and serves as our control experiment.

The second experiment employs the UW PBL scheme, the UW shallow convection scheme and no deep convective parameterization. In this case, precipitation associated with deep convection will only be produced if the full grid cell reaches saturation

ACPD
11, 8385–8430, 2011

(through SCAM microphysical scheme) or if the shallow convection scheme by itself succeeds in producing deep plumes. It can thus be expected that this simulation will underestimate deep convection. The experiment is called UWS and is otherwise identical to the CAM experiment.

Finally, the last set of experiments uses the UW PBL scheme and a modified version of the default UW shallow convection scheme encompassing a unified treatment of shallow and deep convection. Otherwise the integrations are identical in their set-up to CAM and UWS. They are called UWSDpbl, UWSDall, UWSDe0, UWSDe0mf and UWSDe0sq, depending on the modifications made to the UW shallow convection scheme. The modifications are described along the text and in Table 1. Ideally, those simulations should stand in closer agreement to SAM than both the CAM and the UWS integrations.

3 The planetary boundary layer under deep convection

As stated in the introduction, we regard deep convection as shallow convection modified due to its production of heavy precipitation. In this view, the cloud-base mass flux in deep as well as shallow convection is regulated by the PBL and the subcloud mixed layer. Bulk instability measures like Convective Available Potential Energy (CAPE) are relevant to the vertical structure of cumulus convection, which in turn indirectly modifies the thermodynamic structure of the PBL and the overlying air. However, they are not viewed as direct controls on the cloud-base mass flux. This approach is supported by Kuang and Bretherton (2006), who showed that changes in CIN and TKE were closely correlated in large-eddy simulations of an idealized transition from shallow to deep convection and Fletcher and Bretherton (2010), who showed that a closure based on CIN and TKE could predict the cloud-base mass flux in LES simulations of ARM, KWAJEX and BOMEX.

In this section, we thus investigate how changes in the PBL structure between shallow and deep convection, especially due to the evaporation of precipitation, affect

ACPD
11, 8385–8430, 2011

cloud-base mass flux and cloud-base thermodynamic properties. Both are key parameters controlling the convective development. We use the SAM outputs to derive appropriate relations characterizing such effects. Except noted otherwise, all the quantities are averaged horizontally. The derived relations are then implemented in the UW shallow convection scheme and tested in a single-column mode.

3.1 SAM results

3.1.1 Cloud-base mass flux

Figure 1 shows the time series of TKE averaged over the PBL and precipitation at cloud base for ARM and KWAJEX obtained from the SAM simulations. It is evident that TKE increases from shallow to deep convection, i.e. with increasing precipitation. The increase in TKE is driven by the evaporation of precipitation, which generates cold pools that induce horizontal flows. The increase in TKE and the associated organized surface convergence along cold pool boundaries represent a supplementary energy source for lifting an air parcel and thus favor the development of convection, as apparent in our SAM simulations and many past studies of deep convection (see e.g., Rio et al., 2009; Khairoutdinov and Randall, 2006).

The increase in TKE due to cold pool activity is not directly resolved by a coarse-resolution global model. Rio et al. (2009) represented this effect by implementing a density current parameterization and coupling it to the Emanuel (1991)'s scheme. Here we follow a simpler, more empirical, approach to parameterize this effect.

Figure 2 shows a scatter plot of mean TKE in the PBL ($\overline{\text{TKE}}$) versus a measure of evaporative potential (and thus cold pool activity) formed as the product of domain-mean precipitation at the average convective cloud base (RR_{cb}) and the height of the planetary boundary layer (PBLH), for our ARM and KWAJEX simulations. The cloud base is defined following Fletcher and Bretherton (2010) as the lifting condensation level of an air parcel with a potential temperature θ equal to the mean 200–400-m θ and a water vapor mixing ratio q_v equal to the mean 200–400-m $q_{\text{v}} + \sigma_{\text{q}}$, where σ_q is

ACPD
11, 8385–8430, 2011

the horizontal standard deviation in q_v over the same height range. The height of the PBL is diagnosed as the height where the resolved-scale horizontal mean turbulent buoyancy flux reaches its minimum. If the estimated cloud base is lower than the PBL height, we set its value to the height of the PBL, as done in the UW scheme. The full circles in Fig. 2 are for the onset/mature phase in which shallow convection is developing into deep precipitating convection, while open circles are for the decay phase. The times classified into the different phases, subjectively determined from the domain-mean precipitation time series, are indicated in Fig. 1 for reference.

Figure 2 indicates that $\overline{\mathrm{TKE}}$ scales with $RR_{\mathrm{cb}}\cdot$ PBLH. The value for zero precipitation should correspond to the TKE in a dry convective boundary layer $\overline{\mathrm{TKE}_{\mathrm{dry}}}$, which is predicted by the PBL scheme. We can thus write:

$$\overline{\mathrm{TKE}} = \overline{\mathrm{TKE}_{\mathrm{dry}}} + C\cdot RR_{\mathrm{cb}}\cdot \mathrm{PBLH} \quad (1)$$

with $C = 17280\,\mathrm{s}^{-1}$, RR_{cb} in $\mathrm{m\,s}^{-1}$, TKE in $\mathrm{m}^2\,\mathrm{s}^{-2}$ and PBLH in m. The correlation coefficient is 0.92 for KWAJEX and 0.83 for ARM during the onset/mature phase. The larger scatter in ARM results from the larger variability in the sampled synoptic conditions. The agreement worsens during the decay precipitation phase as cold pools need time to dissipate after the evaporation of precipitation is finished.

The evaporation of convective precipitation induces a positive feedback between convection and boundary-layer processes embodied in Eq. (1), because it generates TKE that yields more convection and more precipitation. However, the evaporation of precipitation also cools and stabilizes the PBL. At a certain point, the PBL collapses and shuts down convection. This effect is expressed by the use of PBLH in Eq. (1).

3.1.2 Cloud-base thermodynamic properties

Figure 3 shows example profiles of mass flux as a function of moist static energy (MSE), with mean and saturated MSE for ARM day 178 at 12:00 and 15:00 LT overplotted for reference. The profiles are obtained by binning at each height the grid points by

ACPD
11, 8385–8430, 2011

their MSE and summing their mass flux pro bin (see Kuang and Bretherton, 2006). The bin size is 0.25 K. Light to dark red colors in Fig. 3 imply positive values of the vertical velocity and thus represent updrafts, while light to dark blue colors represent downdrafts. Also, the shaded portion in Fig. 3 above the green line of the saturation MSE represents the cloudy points. We use here MSE as it is moist-adiabatically conserved and determines the temperature in saturated air. It is thus a useful and dynamically relevant characteristic of cumulus updrafts. This conservation is approximate in reality, but is exact (except for ice processes) given the thermodynamic equations employed in SAM. Throughout this paper, MSE is rescaled into temperature units by dividing by $c_p = 1006\,\mathrm{J\,kg^{-1}\,K^{-1}}$. 12:00 LT corresponds to the shallow convection phase, while 15:00 LT illustrates the situation under deep convection. Both panels also indicate the cloud cover profile on the right.

Comparison of Fig. 3a and b reveals similarities and differences in the partitioning of cloud-base MSE between shallow and deep convective updrafts and downdrafts. The cumulus cloud base is visible in both plots as the altitude of maximum lower-tropospheric cloud fraction; at this level the mean updraft MSE is almost identical to the domain-mean saturation MSE, suggesting the cumulus updrafts have nearly the same temperature (and hence buoyancy) as their environment at cloud base. Above cloud base, the net upward mass flux is carried almost exclusively within cumulus clouds. As clouds are less numerous than cloud-free grid points the line of the domain-mean MSE does not pass in-between up- and downdrafts but is shifted towards the environment. The typical range of MSE carried by the upward mass flux is also vertically continuous across cloud base at both times. Before strong precipitation (Fig. 3a), the PBL has a structure akin to the structure of a dry convective boundary layer. Half of the PBL experiences updrafts with slightly higher MSE, half downdrafts with slightly lower MSE. Later on (Fig. 3b), precipitation-driven downdrafts bring a broad range of lower MSE into the PBL. Only the remaining high-MSE part of the PBL contributes to the convective cloud-base updrafts, and the difference between the mean updraft MSE at cloud base and the mean PBL MSE increases.

ACPD
11, 8385–8430, 2011

We find that for both shallow and deep convection, the mean updraft MSE at cloud base (MSE_{cb}) can be parameterized as follows:

$$MSE_{cb} = \overline{MSE} + L/c_p\sigma_q \quad (2a)$$

$$\sigma_q = 5\times10^{-4} RR_{cb}^{0.14+0.024\log(RR_{cb})},\ RR_{cb} > 0.2 \quad (2b)$$

with RR_{cb} given in mm day^{-1}, $\overline{MSE}$ defined as the MSE averaged over the layer 200–400 m, σ_q the horizontal standard deviation in specific humidity over the layer 200–400 m and $L = 2.5\times10^6$ J kg^{-1}. For $RR_{cb} \leq 0.2$ mm day^{-1}, MSE_{cb} is simply set to $\overline{MSE}$, since there is no downdraft-related cooling effect in the PBL under such small precipitation amounts (see Fig. 3a).

The expression in Eq. (2a) is inspired by Fletcher and Bretherton (2010), while Eq. (2b) contains the approximation to compute σ_q. It is obtained by fitting a second-order polynomial in $\log(RR_{cb})$ to $\log(\sigma_q)$. This fit is illustrated in Fig. 4, using points from KWAJEX (full circles), ARM (open circles) and BOMEX (cross). $\log(RR_{cb})$ is chosen as the predictor since the increased PBL variability seems to mainly be due to cold pool formation (see previous section).

3.2 SCAM experiments

We now use the results of the previous Sect. 3.1 to modify cloud-base characteristics of the UW shallow convection scheme to help make it more suitable for deep convection. The new simulation is called UWSDpbl. In contrast to UWS, it employs the mass flux closure developed by Fletcher and Bretherton (2010) based on the same set of LES simulations as we use. This closure, like the default UW shallow cumulus mass flux closure, relates the mass flux to an exponential function of the ratio between CIN and TKE, but multiplies this function by a different prefactor. UWSDpbl uses a convective velocity based on surface fluxes, while UW uses the square root of TKE. This distinction becomes important when cold pools greatly increase the component of TKE

ACPD
11, 8385–8430, 2011

in mesoscale horizontal motions without greatly increasing the turbulent vertical velocity variance. Furthermore, UWSDpbl includes Eq. (1) to predict cold-pool TKE for the mass flux closure. Cloud-base thermodynamic properties are expressed as the mean over the 200–400 m layer plus one standard deviation in humidity σ_q, instead of their surface or minimum values (see Sect. 2.2). σ_q is predicted with Eq. (2b). Finally, the proportionality constant scaling the evaporation rate of falling precipitation is increased from 2×10^{-6} to 1.5×10^{-5} to be consistent with the values obtained from the SAM simulations (not shown).

Figure 5 shows the diurnal cycle of precipitation for ARM days 176, 178, 179 and 180 for the simulations CAM, UWS, UWSDpbl and the SAM LES simulation. Day 174 exhibits similar features but is not included here for brevity. The default CAM configuration shows too weak a diurnal rainfall modulation that causes excessive morning precipitation. This problem is especially visible on day 178, which constitutes the most archetypical example of surface forced convection during the period.

Both UWS and UWSDpbl better capture the timing of precipitation. The onset of precipitation coincides with SAM on days 176, 178 and 180 (Fig. 5a, b, d), while it is delayed on days 179 (Fig. 5c) and 174 (not shown). However, UWS and UWSDpbl also strongly underestimate the precipitation amounts. The cloud-base improvements in UWSDpbl increase the simulated amounts on day 178 but the impact remains generally small. This is understandable; the cloud-base improvements only affect the simulation of strongly precipitating convection; if the convection never produces significant rainfall, these improvements have no chance to modify the simulation.

Hence, the inclusion of precipitation-related modifications in cloud-base properties is insufficient to transform a shallow convection scheme into a realistic deep convection scheme. Analysis of the different days suggests that UWS and UWSDpbl have difficulties in transitioning to precipitating deep convection due to too large entrainment/detrainment rates. We address this problem in the next section.

ACPD
11, 8385–8430, 2011

4 Entrainment

As in the previous section, we first employ the SAM simulations to derive formulations for entrainment and detrainment that work for both shallow and deep convection. We then implement and test them in combination with our cloud-base property modifications with single-column model experiments.

4.1 SAM results

Our approach retains the idea of buoyancy sorting described in Sect. 2.2, in which entrainment and detrainment rates are computed as $\epsilon = \epsilon_0 \chi_c^2$ and $\delta = \epsilon_0 (1 - \chi_c)^2$, but SAM is used to revise the formulation of ϵ_0.

The formulation of ϵ_0 is admittedly empirical and tuned to our SAM simulations, and it would be desirable in the future to use a more theoretically elegant approach tuned against a broader ensemble of simulations and observational constraints. However, our approach does try to build in some theoretically expected relationships between mixing rate and environmental variables. It is based on two main assumptions. The first assumption is that ϵ_0 varies approximately linearly with height over limited height ranges. The second assumption is that for buoyant updrafts more than a couple of hundred meters above their LCL, ϵ_0 correlates inversely with precipitation at cloud base (see e.g., Fig. 7). Covariability between ϵ_0 and precipitation is expected because higher precipitation amounts foster cold pool development which organizes the boundary layer. This produces larger and more coherent updrafts which have a lower bulk-mean entrainment rate near cloud base (see e.g., Kuang and Bretherton, 2006; Khairoutdinov and Randall, 2006). This concept generalizes the specification of an inverse cloud radius as predictor for entrainment rates (as in e.g. Kain, 2004) by allowing this radius to vary based on precipitation. Our approach can produce similar results to decreasing entrainment rate at high ambient relative humidity, a method successfully applied by Bechtold et al. (2008), to the extent that higher environmental relative humidity will correlate with deeper clouds that yield more precipitation.

ACPD
11, 8385–8430, 2011

Relying on these considerations and as schematically shown in Fig. 6, we first specify three "anchor" heights within the cumulus layer

$$z_1 = z_{cb} + 200\ \text{m},\ z_2 = z_{cb} + 1500\ \text{m},\ z_3 = z_{cb} + 3000\ \text{m} \tag{3}$$

We determine ϵ_0 as a piecewise linear function of z between specified values at z_{cb} and the anchor heights:

$$\epsilon_0(z) = \left\{ \begin{array}{ll} \epsilon_0(z_{cb}) + (\epsilon_0(z_1) - \epsilon_0(z_{cb}))(z - z_{cb})/(z_1 - z_{cb}), & z < z_1 \\ \epsilon_0(z_1) + (\epsilon_0(z_2) - \epsilon_0(z_1))(z - z_1)/(z_2 - z_1), & z_1 < z < z_2 \\ \max(\epsilon_0(z_2) + (\epsilon_0(z_3) - \epsilon_0(z_2))(z - z_2)/(z_3 - z_2), \epsilon_0^{min}), & z > z_2 \end{array} \right\} \tag{4}$$

Lastly, the mixing rates ϵ_0 at cloud base and at the anchor heights are empirically chosen based on theoretical considerations and the SAM simulations as follows:

$$\epsilon_0(z_{cb}) = 4.1 \times 10^{-3}/(\rho_{cb} g w_{cb}) \tag{5}$$

$$\epsilon_0(z_1) = \epsilon_0(z_{cb}) + (2.75 \times 10^{-4}(\max(RR_{cb}, 5))^{-0.3} - \epsilon_0(z_{cb}))(z_1 - z_{cb})/(z_2 - z_{cb}) \tag{6}$$

$$\epsilon_0(z_2) = 2.75 \times 10^{-4}(\max(RR_{cb}, 0.1))^{-0.3} \tag{7}$$

$$\epsilon_0(z_3) = 1.84 \times 10^{-4}(\max(RR_{cb}, 0.1))^{-0.2} \tag{8}$$

In these formulas, ϵ_0 is in Pa^{-1}, RR_{cb} in mm day^{-1}, w_{cb} is the updraft velocity at cloud base (m s^{-1}), ρ_{cb} is air density at cloud base (kg m^{-3}) and g is gravity.

Mixing processes in a cumulus updraft are thus divided into three main layers: a cloud-base layer between z_{cb} and z_1, a transition layer between z_1 and z_2 and a deep layer between z_2 and the top of the cloud z_{ct} with $z_{ct} \geq z_3$.

The cloud-base layer characterizes the thin layer near cloud base where the boundary layer plumes reach saturation. It is constantly fed by new plumes rising from the PBL. Its thickness is set to 200 m to ensure that it encompasses at least two model levels even in climate simulations with coarse vertical resolution; making this layer too thin can induce numerical instability.

ACPD
11, 8385–8430, 2011

The mixing rate in the transition layer helps determine whether the cloud remains shallow or transitions to deep convection. The top of this layer z_2 is chosen to be 1500 m above cloud base, a representative cloud depth for achieving significant precipitation. The mixing rate $\epsilon_o(z_2)$ is tied to precipitation; if the bulk updraft doesn't reach z_2 a lower rain rate threshold of 0.1 mm day^{-1} is used in calculating the mixing rate.

Finally, the top layer contains the deeper, heavily precipitating updrafts.

Figure 7 shows scatter plots supporting the relationships needed to determine ϵ_0 at cloud base and the anchor heights z_2 and z_3. Beginning from the top of the cloud and thus from Fig. 7b, c and corresponding Eqs. (7)–(8), $\epsilon_0(z_2)$ and $\epsilon_0(z_3)$ are set proportional to the inverse of the precipitation at cloud base (see above). The correlation coefficient amounts to 0.6 in both cases. An upper bound, obtained in Eqs. (7) and (8) by setting $RR_{\mathrm{cb}} = 0.1\,\mathrm{mm\,day^{-1}}$, is set on $\epsilon_0(z_2)$ and $\epsilon_0(z_3)$ to avoid large values for small precipitation amounts. Lastly, we enforce a lower bound $\epsilon_o^{\mathrm{min}} = 5\times10^{-5}$ Pa^{-1} on $\epsilon_o(z, z > z_2)$. This is a typical value for the mixing rate estimated from SAM at higher levels within deep convective updrafts.

Note that Fig. 7b only includes the onset/mature precipitation phase, as marked in Fig. 1, to determine $\epsilon_0(z_2)$. During the decay phase, precipitation amounts are small, like in the onset phase, but mixing rates are small. Including those points in the regression reduces the slope of the regression line and results in too small mixing rates during the onset phase. This manifests itself by an overly rapid transition to deep convection in the single-column model experiments. The overestimation implied by Eq. (7) for the decay phase does not seem to have any detrimental effect on the simulations.

At the anchor height z_1, ϵ_0 is chosen in a way to allow a smooth transition between the cloud base layer, where ϵ_0 tends to decrease with height, and the transition layer. For $RR_{\mathrm{cb}} \geq 5\,\mathrm{mm\,day^{-1}}$, Eq. (6) implies a constant linear change in mixing rate with height between z_{cb} and z_2. For smaller precipitation amounts, $\epsilon_0(z_1)$ is simply bounded to the value obtained at that height for $RR_{\mathrm{cb}} = 5\,\mathrm{mm\,day^{-1}}$. The choice of a threshold of 5 mm day^{-1} is somewhat arbitrary and may be seen as a tuning parameter. Larger

ACPD
11, 8385–8430, 2011

values will delay the transition to deep convection and vice versa.

Finally at cloud base ϵ_0 is chosen proportional to the velocity at cloud base, as indicated in Fig. 7a and corresponding Eq. (5). The correlation coefficient is 0.8. We do not use RR_{cb} as a supplementary predictor since it does not add significant skill to this regression. This is analogous to the approach of Neggers et al. (2002), who proposed $\epsilon = 1/(w_u \tau_c)$, where w_u is the updraft velocity (m s^{-1}) and $\tau_c = 300$ s is an empirical mixing timescale. In fact, our formulation would imply $\epsilon = 4.1 \times 10^{-3} \chi_c^2 / w_{cb}$, which yields the same result for a typical cloud-base value $\chi_c = 0.9$.

We also note that for values $w_{cb} = 0.5\,\mathrm{m\,s^{-1}}$ and $z_{cb} = 500$ m typical of BOMEX, our formulation implies $\epsilon_0 = 8 \times 10^{-3} \mathrm{m}^{-1} = 4/z_{cb}$, which is at the low end of the range of possible cloud-base values given in Table 1 of Park and Bretherton (2009) for the default UW scheme.

4.2 SCAM experiments

The revised entrainment-detrainment formulation is tested in SCAM by introducing it into UWSDpbl. Two other changes are made to the default mixing scheme. First, no water is detrained before performing buoyancy sorting. Second χ_c is limited to a maximum value of 0.5 above 6 km to avoid the development of instabilities due to compensating subsidence in cases of an increasing mass flux with height. The new simulation is called UWSDall (see Table 1).

Figure 8 shows the diurnal cycle of precipitation for ARM days 176, 178, 179 and 180 for UWSDall, CAM, UWS and SAM. Comparison to Fig. 5 reveals a strong impact of the new entrainment formulation. UWSDall produces stronger precipitation than UWSDpbl. The amounts are of comparable magnitude to the SAM simulation. Despite a tendency to produce too large precipitation amounts at the beginning of the onset phase, UWSDall clearly improves the simulated precipitation diurnal cycle as compared to CAM. This is especially true on day 178 (see Fig. 8b), where most convective parameterizations would fail (see Guichard et al., 2004).

ACPD
11, 8385–8430, 2011

UWSDall, in contrast to UWSDpbl, can realistically transition to deep convection. In principle, the moistening of the environment during the day through detrainment from previous shallow convection should increase χ_c, so the mass flux decreases less rapidly with height and at some point significant mass flux reaches into the mid-troposphere. Nevertheless this effect did not appear sufficient in our single-column model experiments, in contrast to results from cloud-resolving studies (see especially Chaboureau et al., 2004). An additional and explicit sensitivity of fractional entrainment and detrainment rates to precipitation is required for the UW scheme to realistically transition from shallow to deep convection with the right diurnal timing.

Figure 9a–d shows cloud cover, mass flux, relative humidity and temperature profiles for UWSDall, CAM, UWS and SAM on day 178 averaged over the precipitation phase (10:00 to 18:00 LT). CAM simulates excessive cloud cover at all levels (see Fig. 9a) and an unrealistic mass flux profile (see Fig. 9b) compared to SAM. UWSDall underestimates the cloud cover above 5 km (this result is sensitive to the chosen relative humidity threshold for the onset of stratiform cloud formation), but the mass flux profile is much more similar to SAM, with only a slight remaining underestimate of mass flux between 1.5 and 8 km. This good agreement implies that the new entrainment formulation is able to capture typical entrainment and detrainment rate profiles in ARM. Similar conclusions hold for other times and ARM days.

In terms of relative humidity and temperature, Fig. 9c, d indicates that UWSDall outperforms CAM and UWS. The UWSDall curve tends to agree well with the SAM results. The relative performance of the simulations is case-dependent. Significant improvements are obtained on days 178 and 179 (in which the diurnal cycle of surface fluxes is the main convective forcing) while all simulations perform similarly on the remaining days, on which large-scale advective forcing is more important (not shown).

One of the main biases of the simulations is visible in Fig. 9d and especially in Fig. 9e. Figure 9e shows specific humidity profiles at 15:00 LT, the time of maximum precipitation. CAM, UWSDall and UWS are all moister than SAM. They all exhibit a well-mixed boundary layer (see profile below about 1 km), while SAM only remains well

ACPD
11, 8385–8430, 2011

mixed in the upper part of the PBL (between about 300–900 m).

This bias is a fundamental consequence of the interaction of the boundary layer scheme with the deep convection. Both the UW PBL scheme and Holtslag and Boville (1993) do not consider horizontal heterogeneity within the boundary layer. To maintain convection, they must sustain a convective PBL that extends from the surface to the convective cloud base, or else the CIN will become too large to allow further cloud-base mass flux. The convective PBL must be nearly well mixed. On the other hand, the SAM humidity profile is due to cold pools in which moist, cool air spreads out along the surface in some parts of the domain, while updrafts are driven by surface fluxes and organized surface convergence in other parts of the domain.

Figure 10 finally shows time series of MSE averaged over the lowest 1 km for ARM and serves to illustrate the other main deficiency of the single-column model experiments. All the SCAM simulations exhibit warmer MSE than SAM during the phase of heavy precipitation (compare to the precipitation time series in Fig. 8). The apparent missing stabilization of PBL MSE in SCAM is a direct consequence of not having explicit downdrafts in UWS and UWSD. CAM does include downdrafts, but only saturated downdrafts. Yet most of the downdrafts appear to be unsaturated in SAM.

Note that even if UWSD does not contain explicit downdrafts, the simulation still can track precipitation and exhibit some reduction in MSE with time. The effects are larger in UWSD than in UWS indicating that the modifications performed to the convection scheme can indeed introduce a feedback between convective rainfall and changes in the boundary layer structure: at first they help triggering convection by increasing TKE, while later on they help shutting down convection (see Sects. 3.1 and 4.3). This feedback may be partly achieved via changes in PBL ventilation between UWSD and UWS. The reported biases in MSE, especially towards the end of the different days, have no strong influence since we used prescribed large-scale forcing and since we simulated each day separately.

Figure 11 displays the results obtained for KWAJEX for the different simulations. We do not show precipitation since all the simulations perform well due to the use of a

ACPD
11, 8385–8430, 2011

prescribed omega field. The different profiles in Fig. 11 have been averaged over the full time period. As in ARM we can recognize the improvements in the simulated cloud cover and mass flux profiles in UWSDall as compared to CAM and UWS. UWSDall also captures the relative humidity profile very well, while both CAM and UWS tend to overmoisten the troposphere, especially above 3 and 1 km, respectively. Finally, no strong biases can be detected in the simulated temperature profile in UWSDall.

As in ARM, Fig. 11e reveals the bias toward a well-mixed PBL in the SCAM simulations. CAM and UWSDall appear too cold and too dry, while they were too warm and too moist in ARM (Fig. 9d, e). Time series of mean PBL MSE (not shown) reveals that the depletion of MSE in CAM and UWSDall during the precipitating phase is similar both in ARM and KWAJEX. Since the depletion is much stronger in SAM in ARM than in KWAJEX due to stronger downdrafts, this results in a warm and moist (cold and dry) bias in ARM (KWAJEX). We thus conclude that the ventilation of the PBL is too strong in UWSDall, which partly compensates for the missing downdrafts. In opposition, UWS never exhibits a strong depletion in MSE and thus is characterized by a warm and moist bias in all the cases.

The results for BOMEX are finally displayed in Fig. 12 with profiles of liquid water potential temperature, total specific humidity, cloud cover and mass flux for UWS, CAM, UWSDall and SAM. The profiles have been averaged over hours 3 to 6 of the BOMEX integrations, as in Park and Bretherton (2009). CAM exhibits similar biases to those noted in Park and Bretherton (2009) with excessive cloud cover throughout the cumulus layer. This bias is mainly removed in UWS and UWSDall. Although differences exist in the simulated profiles between UWS and UWSDall in Fig. 12, UWSDall is still able to simulate a typical case of shallow convection as well as UWS. In particular, with UWSDall, as with UWS, the simulated clouds remain shallow. Employing the Zhang and McFarlane (1995) scheme as sole convective parameterization in CAM would erroneously simulate some deep convection for BOMEX.

Hence in terms of large-scale variables UWSDall agrees well with SAM in many respects. It provides improved single-column simulations of tropical oceanic, mid-latitude

ACPD
11, 8385–8430, 2011

continental and shallow convection than the default version of the CAM model. It also gives more realistic simulations than UWS of both deep convection cases.

4.3 Sensitivity

In the previous section, we demonstrated that UWSDall compares better to SAM than either CAM or UWS. However, it remains to be shown whether all the included modifications are important for these improvements. From the results in Sect. 3 it is clear that the mixing rates need to be reformulated. The necessity of the changes in cloud-base mass flux and cloud-base thermodynamic properties are investigated in this section.

To that aim we perform three sensitivity experiments called UWSDe0, UWSDe0mf, and UWSDe0sq (see Table 1). UWSDe0 is identical to UWSDall except that it only includes entrainment/detrainment effects, not the modifications to cloud-base mass flux (Eq. 1) and thermodynamic properties (Eqs. 2a, b). UWSDe0mf and UWSDe0sq build on UWSDe0: UWSDe0mf adds only the changes in cloud-base mass flux (Eq. 1), while UWSDe0sq adds only the changes in cloud-base thermodynamic properties (Eqs. 2a, b) via changes in σ_q.

Figure 13 shows the corresponding time series of precipitation for the ARM days 176, 178, 179 and 180. The differences between UWSDe0, UWSDe0mf and UWSDe0sq are larger on days 178–179, which are dominated by surface flux forcing, than on days 176 and 180 (and in the KWAJEX simulation), which have stronger advective forcing. All simulations initiate convection at the same time, which is expected since both cloud-base changes only affect the parameterization when there is already convective rainfall. However for days 178–179, all three new cases produce a period of rainfall with too weak a maximum and lasting too long compared to both SAM and UWSDall. We conclude that both cloud-base changes are required to make a sufficiently strong positive feedback between convective rainfall and changes in the boundary layer structure.

The increase in precipitation in UWSDe0mf and UWSDe0sq versus UWSDe0 follows from an increased mass flux at all heights. This stands in better agreement to the SAM

ACPD
11, 8385–8430, 2011

values (not shown). The enhanced mass flux in UWSDe0mf is a direct consequence of both enhanced cloud-base mass flux and more frequent triggering of convection, as expected from Eq. (1). The enhanced mass flux in UWSDe0sq follows from an enhanced entrainment rate and decreased detrainment rate at cloud base, which thus allow more plumes to be retained in the updraft. The latter changes in ϵ and δ relate to a value of χ_c larger in UWSDe0sq than in UWSDe0, as expected from the use of moister updraft parcels.

For most other variables, the differences between UWSDe0mf, UWSDe0sq and UWSDe0 are small, both in ARM and KWAJEX. The exceptions are of course the TKE values and the cloud-base thermodynamic properties.

Figure 14 displays scatter plots of mean PBL TKE in SCAM versus SAM for the ARM, KWAJEX and BOMEX cases. On the left, we show UWS as an example for the simulations which do not include the TKE increase due to cold pool activity (i.e., UWS, UWSDe0, UWSDe0sq). On the right, UWSDall is chosen as an example for the two remaining simulations, where Eq. (1) is used.

As indicated by Fig. 14 and as expected, TKE is strongly underestimated in UWS (or equivalently UWSDe0 and UWSDe0sq), while UWSDall (and UWSDe0mf) are in better agreement with SAM. The latter two simulations are able to capture the increase in TKE during precipitation events and thus confirm the appropriateness of Eq. (1). The overall underestimation in Fig. 14b is due to a slight underestimation of the boundary layer height in UWSDall. The points where a strong discrepancy between SCAM and SAM values remains visible in Fig. 14b correspond to those times where UWSDall produces no or only weak precipitation, while SAM records strong precipitation.

In terms of cloud-base thermodynamic properties, the use of Eq. (2b) yields an increase in cloud-base MSE. This increase amounts up to 2 K in UWSDe0sq (and UWSDall) with respect to UWSDe0 (or UWS, UWSDe0mf). Given the existing biases in the PBL (see Sect. 4.2) this agrees better with SAM for KWAJEX, but less well for ARM.

ACPD
11, 8385–8430, 2011

5 Conclusions

This study was geared towards improving the simulation of deep convection with coarse-resolution climate models. The aim was to develop and assess the suitability of a unified convection scheme, capable of handling both shallow and deep convection. Our approach is based on the hypothesis that the main difference between shallow and deep convection is precipitation, so that improving the representation of some key effects of precipitation in a shallow convection scheme can allow it to be extended into a unified scheme.

We considered previously studied cases of shallow convection (BOMEX), tropical oceanic convection (KWAJEX) and mid-latitude continental convection (ARM). We used large-eddy simulations of the three cases as benchmarks for parameterization formulation and improvement. We implemented our improved relations in the UW shallow convection scheme and tested the results in the SCAM single-column modeling framework.

We included three main effects of precipitation on convective development, encompassing cloud-base mass flux, cloud-base humidity and entrainment/detrainment rates. Evaporation of precipitation generates cold pools in the PBL, forcing convergence and thus favoring cloud formation. This expresses itself by an increase in boundary-layer TKE, which in the UW scheme is a primary control on cloud-base mass flux. We found that the increase of TKE compared to dry convective boundary layer scales with precipitation at cloud base times the height of the PBL. Evaporation of precipitation also modifies the probability distribution function of cloud-base thermodynamic properties, increasing horizontal humidity variance. Cumulus updrafts tend to form over the moister parts of the PBL, so to predict cumulus base humidity we explicitly include a parameterization of humidity variance in terms of cloud-base precipitation rate. Finally, the formation of cold pools organizes the planetary boundary layer and the entire cumulus ensemble and indirectly lowers the bulk entrainment rate ϵ_0. This effect is represented through a dependence of the cumulus updraft lateral mixing rate to pre-

ACPD
11, 8385–8430, 2011

cipitation at cloud base (see Eqs. 3 to 8).

These modifications were implemented in the UW shallow convection scheme, tested in a single-column version of CAM, and compared with LES, as well as to the default CAM version and to a CAM version employing the default UW shallow convection scheme without any deep convective parameterization.

In all cases, the new scheme performs as well as or better than the default CAM version. It also outperforms the simulations using the default UW shallow convection scheme as the sole convective parameterization. For our tropical oceanic convection case, the new unified scheme especially improves relative humidity, cloud cover and mass flux profiles. The performance in terms of mid-latitude continental convection is more case-dependent. The main improvement is in the simulated timing of the diurnal cycle when surface fluxes are the dominant forcing for convection. The new unified scheme removes the premature onset of precipitation, which is a common pitfall of deep convective parameterizations, and is able to simulate the peak rainfall rate and duration of rainfall reasonably well. Finally, the scheme can still realistically simulate shallow oceanic trade-cumulus convection.

The main biases, which are present not only with the new scheme but in all of our single-column model experiments, are that the simulated PBL structure tends both to be too well-mixed and to insufficiently reduce boundary-layer MSE during deep convection as compared to LES, especially for mid-latitude continental convection. We attribute those biases to a combination of two factors. First, the PBL schemes do not consider rain-induced horizontal heterogeneity within the boundary layer. To maintain convection, they must sustain a convective PBL that extends from the surface to the convective cloud base. Second, the UW convection scheme does not explicitly consider downdrafts, while the Zhang and McFarlane (1995) scheme only includes saturated downdrafts. Yet most of the downdrafts appear to be unsaturated in the LES.

Of the three tested modifications (i.e., in cloud-base mass flux, cloud-base thermodynamic properties and bulk entrainment rate), changing the bulk updraft lateral mixing rate has the largest impact. Without this, the UW scheme has difficulty in simulating a

ACPD
11, 8385–8430, 2011

realistic transition from shallow to deep convection. This is true even though its buoyancy sorting algorithm should allow it to be sensitive to free-tropospheric relative humidity and previous cloud-resolving modeling studies (e.g., Chaboureau et al., 2004) have indicated that moistening of the troposphere through detrainment from shallow and/or congestus clouds controls the transition to deep convection. Expressed in other words, precipitation (or its evaporation) is a strong positive feedback in the transition from shallow to deep convection in our single-column model experiments, which helps explain why this transition is rather difficult for cumulus parameterizations to simulate. The impacts of our modifications made to the cloud-base mass flux and cloud-base thermodynamic properties are subtler. Separately, they only have small impacts but taken together, they enhance the sensitivity of convection to prior precipitation and enhance the precipitation peaks. Their inclusion seems especially important for the timing and amplitude of the convective diurnal cycle over mid-latitude continental areas.

It thus appears that a unified formulation of shallow to deep convection is possible by including precipitation effects, thus confirming our working hypothesis. Key unresolved issues remain the formulation of unsaturated downdrafts and a better theoretical foundation for formulating appropriate entrainment/detrainment rates, both issues with which deep convective parameterizations have been struggling for a long time. As a next step, global climate model simulations with CAM will be performed with the new unified scheme.

Acknowledgements. The authors would like to thank Peter Blossey for the SAM simulations. The first author was funded by the Swiss National Science Foundation under the fellowship program for advanced researchers, project PA00P2_124153. Chris Bretherton was funded by NSF grant ATM 0425247 to the CMMAP Science and Technology Center.

ACPD
11, 8385–8430, 2011

References

Arakawa, A.: The cumulus parameterization problem: Past, present, and future, J. Climate, 17, 2493–2525, 2004. 8387

Arakawa, A. and Schubert, W. H.: Interaction of a cumulus cloud ensemble with large-scale environment. Part 1, J. Atmos. Sci., 31, 674–701, 1974. 8387

Bechtold, P., Chaboureau, J. P., Beljaars, A., Betts, A. K., Kohler, M., Miller, M., and Redelsperger, J. L.: The simulation of the diurnal cycle of convective precipitation over land in a global model, Q. J. Roy. Meteorol. Soc., 130, 3119–3137, 2004. 8387

Bechtold, P., Kohler, M., Jung, T., Doblas-Reyes, F., Leutbecher, M., Rodwell, J., Vitart, F., Balsamo, G.: Advances in simulating atmospheric variability with the ECMWF model: From synoptic to decadal time-scales, Q. J. Roy. Meteorol. Soc., 134, 1337–1351, 2008. 8387, 8400

Blossey, P. N., Bretherton, C. S., Cetrone, J.: Cloud-resolving model simulations of KWAJEX: Model sensitivities and comparisons with satellite and radar observations, J. Atmos. Sci., 64, 1488–1508, 2007. 8392

Bretherton, C. S.: Challenges in Numerical Modeling of Tropical Circulations. In The Global Circulation of the Atmosphere, edited by: Schneider, T. and Sobel, A. H., Princeton University Press, USA, 302–330, 2007. 8386

Bretherton, C. S. and Park, S.: A new moist turbulence parameterization in the Community Atmosphere Model, J. Climate, 22, 3422–3448, 2009. 8390, 8416

Bretherton, C. S., McCaa, J. R., and Grenier, H.: A new parameterization for shallow cumulus convection and its application to marine subtropical cloud-topped boundary layers. Part I: Description and 1D results, Mon. Weather Rev., 132, 864–882, 2004. 8388, 8390

Chaboureau, J. P., Guichard, F., Redelsperger, J. L., and Lafore, J. P.: The role of stability and moisture in the diurnal cycle of convection over land, Q. J. Roy. Meteorol. Soc., 130, 3105–3117, 2004. 8404, 8411

Chikira, M. and Sugizama, M.: A cumulus parameterization with state-dependent entrainment rate. Part I: Description and sensitivity to temperature and humidity profiles, J. Atmos. Sci., 67, 2171–2193, 2010. 8387

Collins, W. D., and coauthors: The formulation and atmospheric simulation of the Community Atmosphere Model Version 3 (CAM3), J. Climate, 19, 2144–2161, 2006. 8389

Dai, A. G., Giorgi, F., and Trenberth, K. E.: Observed and model-simulated diurnal cycles of

ACPD
11, 8385–8430, 2011

precipitation over the contiguous United States, J. Geophys. Res., 104, 6377–6402, 1999. 8387
Deardorff, J. W.: Usefulness of liquid-water potential temperature in a shallow-cloud model, J. Appl. Meteor., 15, 98–102, 1976. 8390
Deng, L. P. and Wu, X. Q.: Effects of convective processes on GCM simulations of the Madden-Julian Oscillation, J. Climate, 23, 352–377, 2010. 8387
Emanuel, K. A.: A scheme for representing cumulus convection in large-scale models, J. Atmos. Sci., 48, 2313–2335, 1991. 8387, 8395
Fletcher, J. K. and Bretherton, C. S.: Evaluating boundary layer-based mass flux closures using cloud-resolving model simulations of deep convection, J. Atmos. Sci., 67, 2212–2225, 2010. 8394, 8395, 8398
Grandpeix, J. Y., Lafore, J. P., and Cheruy, F.: A density current parameterization coupled with Emanuel's convection scheme. Part II: 1D simulations, J. Atmos. Sci., 67, 898–922, 2010. 8387
Guichard, F, Petch, J. C., Redelsperger, J. L., Bechtold, P., Chaboureau, J. P., Cheinet, S., Grabowski, W., Grenier, H., Jones, C. G., Kohler, M., Piriou, J. M., Tailleux, R., Tomasini, M.: Modelling the diurnal cycle of deep precipitating convection over land with cloud-resolving models and single-column models, Q. J. Roy. Meteorol. Soc., 130, 3139–3172, 2004. 8388, 8403
Hack, J. J.: Parameterization of moist convection in the National Center for Atmospheric Research Community Climate Model (CCM2), J. Geophys. Res., 99, 5551–5568, 1994. 8389, 8393, 8416
Hack, J. J. and Pedretti, J. A.: Assessment of solution uncertainties in single-column modeling frameworks, J. Climate, 13, 352–365, 2000. 8389
Holtslag, A. A. M. and Boville, B. A.: Local versus nonlocal boundary layer diffusion in a global climate model, J. Climate, 6, 1825–1842, 1993. 8389, 8393, 8405, 8416
Kain, J. S.: The Kain-Fritsch convective parameterization: an update, J. Clim. Appl. Meteorol., 43, 170–181, 2004. 8400
Khairoutdinov, M. F. and Randall, D. A.: Cloud Resolving Modeling of the ARM Summer 1997 IOP: Model Formulation, Results, Uncertainties, and Sensitivities, J. Atmos. Sci., 60, 607–625, 2003. 8389, 8392
Khairoutdinov, M. F. and Randall, D. A.: High-resolution simulation of shallow-t-deep convection transition over land, J. Atmos. Sci., 63, 3421–3436, 2006. 8395, 8400

ACPD
11, 8385–8430, 2011

Kuang, Z. and Bretherton, C. S.: A mass-flux scheme view of a high-resolution simulation of a transition from shallow to deep cumulus convection, J. Atmos. Sci., 63, 1895–1909, 2006. 8394, 8397, 8400

Lee, M. I., Schubert, S. D., Suarez, M. J., Held, I. M., Lau, N. C., Ploshay, J. J., Kumar, A., Kim, H. K., and Schemm, J. K. E: An analysis of the warm-season diurnal cycle over the continental United States and northern Mexico in general circulation models, J. Hydrometeorol., 8, 344–366, 2007. 8387

Li, L. J., Wang., B., Wang, Y. Q., and Wan, H.: Improvements in climate simulation with modifications to the Tiedtke convective parameterization in the grid-point atmospheric model of IAP LASG (GAMIL), Adv. Atmos. Sci., 24, 323–335, 2007. 8387

Lin, J. L.: The double-ITCZ problem in IPCC AR4 coupled GCMs: Ocean-atmosphere feedback analysis, J. Climate, 20, 4497–4525, 2007. 8386

Neale, R., Richter, J. R., and Jochum, M.: The impact of convection on ENSO: From a delayed oscillator to a series of events, J. Climate, 21, 5904–5924, 2008. 8387, 8389

Neggers, R. A. J., Siebesma, A. P., and Jonker H. J. J.: A multiparcel model for shallow cumulus convection, J. Atmos. Sci., 1655–1668, 2002. 8403

Park, S. and Bretherton, C. S.: The University of Washington shallow convection and moist turbulence schemes and their impact on climate simulations with the Community Atmosphere Model, J. Climate, 22, 3449–3469, 2009. 8388, 8390, 8403, 8406, 8416

Plant, R. S.: A review of the theoretical basis for bulk mass flux convective parameterization, Atmos. Chem. Phys., 10, 3529–3544, doi:10.5194/acp-10-3529-2010, 2010. 8387

Randall, D. A., Khairoutdinov, M., Arakawa, A., and Grabowski, W.: Breaking the cloud parameterization deadlock, B. Am. Meteorol. Soc., 84, 1547–1564, 2003. 8387

Richter, J. R. and Rasch, P. J.: Effects of convective momentum transport on the atmospheric circulation in the Community Atmospheric Model, version 3 (CAM3), J. Climate, 21, 1487–1499, 2008. 8387, 8389

Rio, C., Hourdin, F., Grandpeix, J. Y., and Lafore, J. P.: Shifting the diurnal cycle of parameterized dep convection over land, Geophys. Res. Lett., 36, 2212–225, 2009. 8387, 8395

Siebesma, A. P. and Coauthors: A large-eddy simulation intercomparison study of shallow cumulus convection, J. Atmos. Sci., 60, 1201–1219, 2003. 8392

Slingo, J. M., Sperber, K. R., Boyle, J. S., Ceron, J. P., Dix, M., Dugas, B., Ebisuzaki, W., Fyfe, J., Gregory, D., Gueremy, J. F., Hack, J., Harzallah, A., Inness, P., Kitoh, A., Lau, W. K. M., McAvaney, B., Madden, R.,Matthews, A., Palmer, T. N., Park, C. K., Randall, R., and Renno,

ACPD
11, 8385–8430, 2011

N.: Intraseasonal oscillations in 15 atmospheric general circulation models: Results from an AMIP diagnostic subproject, Clim. Dynam., 12, 325–257, 1996. 8386

Wang, Y. Q., Zhou, L., and Hamilton, K.: Effect of convective entrainment/detrainment on the simulation of the tropical precipitation diurnal cycle, Mon. Weather Rev., 135, 567–585, 2007. 8387

Yang, G. Y. and Slingo, J.: The diurnal cycle in the Tropics, Mon. Weather Rev., 129, 784–801, 2001. 8387

Zhang, B. J. and McFarlane, N. A.: Sensitivity of climate simulations to the parameterization of cumulus convection in the Canadian Climate Centre general circulation model, Atmos.-Ocean, 33, 407–446, 1995. 8389, 8393, 8406, 8410, 8416

Zhang, G. J. and Mu, M. Q.: Simulation of the Madden-Julian oscillation in the NCAR CCM3 using a revised Zhang-McFarlane convection parameterization scheme, J. Climate, 18, 4046–4064, 2005.

8387

ACPD

11, 8385–8430, 2011

Table 1. Overview of the different SCAM simulations. HB stands for Holtslag and Boville (1993), Hack for Hack (1994), ZM for Zhang and McFarlane (1995), UWPBL for the University of Washington PBL scheme (Bretherton and Park, 2009) and UW for the default University of Washington shallow convection scheme (Park and Bretherton, 2009). UWunif corresponds to the new unified convection scheme.

Name	PBL	Shallow Cu	Deep Cu	Mass flux Eq. (1)	σ_q Eqs. (2a, b)	Entrainment Eqs. (3–8)
CAM	HB	Hack	ZM			
UWS	UWPBL	UW	None	No	No	No
UWSDall	UWPBL	UWunif	UWunif	Yes	Yes	Yes
UWSDpbl	UWPBL	UWunif	UWunif	Yes	Yes	No
UWSDe0	UWPBL	UWunif	UWunif	No	No	Yes
UWSDe0mf	UWPBL	UWunif	UWunif	Yes	No	Yes
UWSDe0sq	UWPBL	UWunif	UWunif	No	Yes	Yes

ACPD
11, 8385–8430, 2011

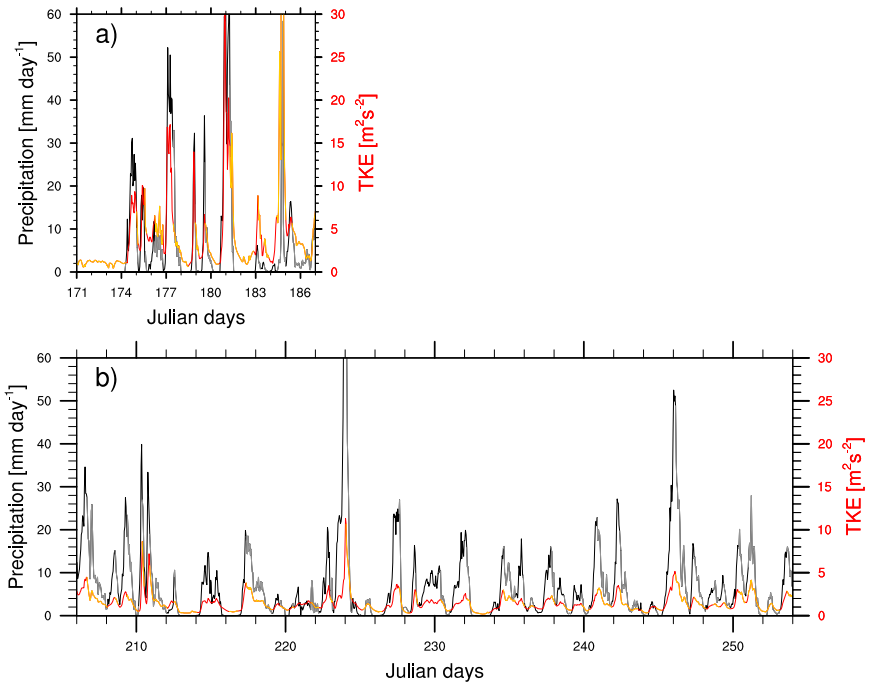

Fig. 1. Time series of precipitation at cloud base; black curve for onset and mature precipitation phase, grey for decay phase, and turbulent kinetic energy averaged over the planetary boundary layer; red curve for onset and mature phase; orange for decay phase, for **(a)** ARM and **(b)** KWAJEX.

ACPD
11, 8385–8430, 2011

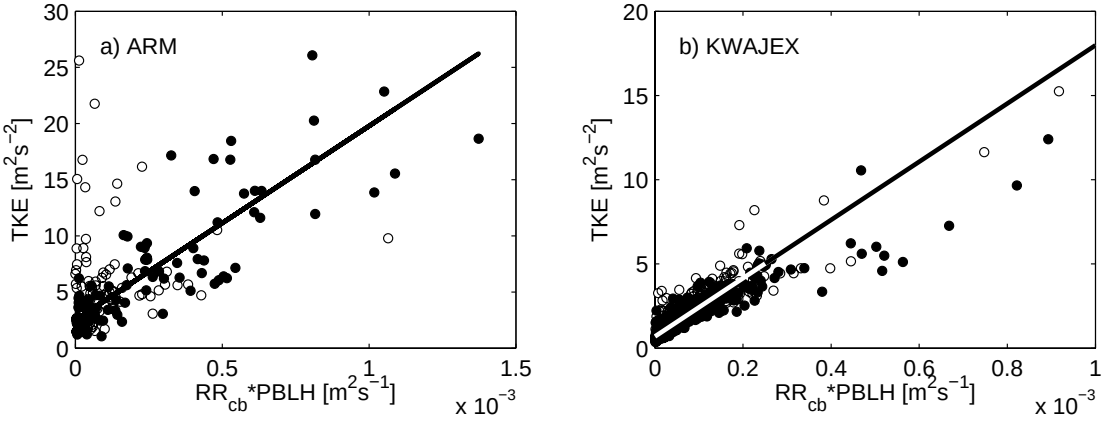

Fig. 2. Scatter plots of mean TKE in the PBL versus RR_{cb}· PBLH for **(a)** ARM and **(b)** KWAJEX. Full circles are for onset and mature precipitation phase, open circles for the decay phase. Onset, mature and decay phases are distinguished in Fig. 1. Slope of the solid regression line in **(a)** and **(b)** is 17 280 s^{-1}.

ACPD
11, 8385–8430, 2011

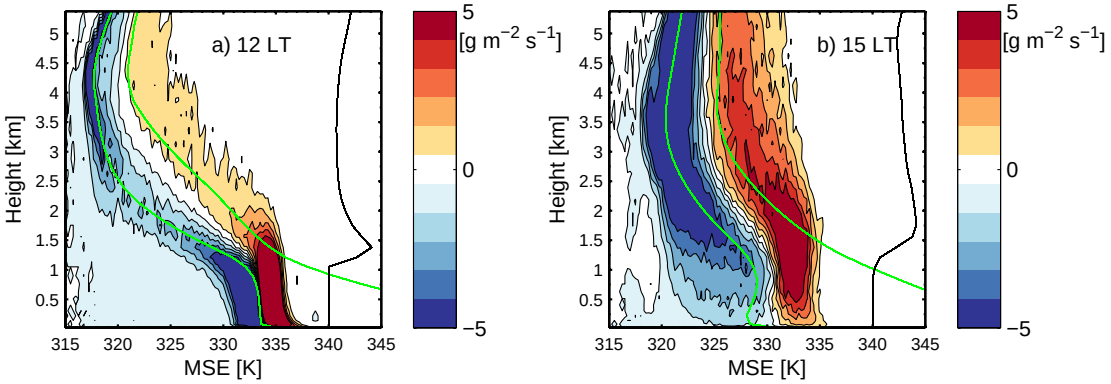

Fig. 3. Profiles of mass-flux binned MSE for ARM day 178 at **(a)** 12:00 and **(b)** 15:00 LT (local time). Green lines represent domain-averaged MSE (K) and saturation MSE (K). Solid line indicates the profile of cloud fraction.

ACPD
11, 8385–8430, 2011

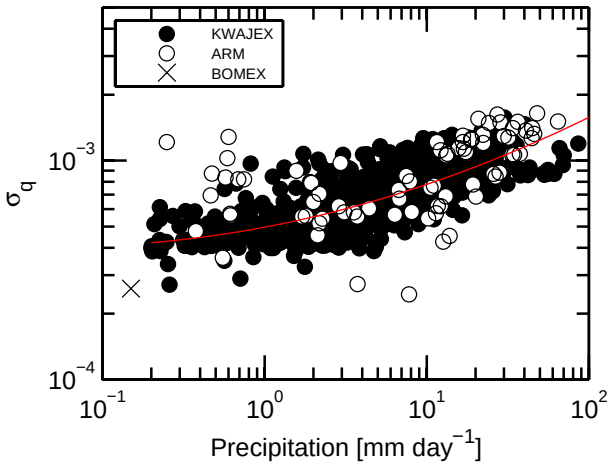

Fig. 4. Log-log plot of σ_q versus precipitation at cloud base for KWAJEX (full circles), ARM (open circles) and BOMEX (cross). The red line denotes the best second-order polynomial fit through the points (see Eq. 2b).

ACPD
11, 8385–8430, 2011

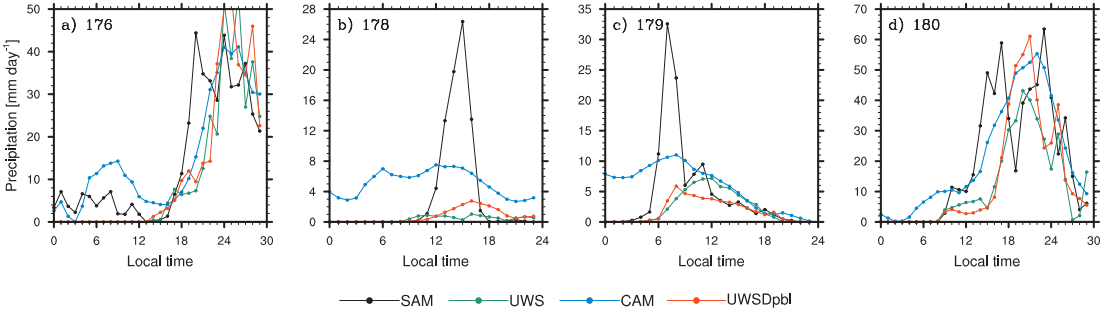

Fig. 5. Diurnal cycle of precipitation for ARM day **(a)** 176, **(b)** 178, **(c)** 179, and **(d)** 180. Black, green, blue and red lines are for SAM, UWS, CAM and UWSDpbl, respectively.

ACPD
11, 8385–8430, 2011

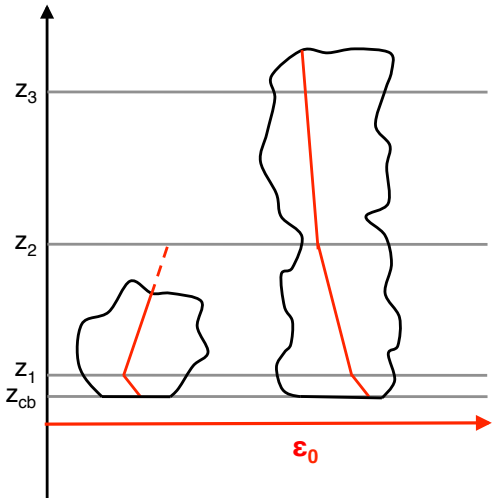

Fig. 6. Schematic view of the determination of ϵ_0 (in red) for a shallow and a deep cumulus updraft. See text and especially Eqs. (3)–(8) for detail.

ACPD
11, 8385–8430, 2011

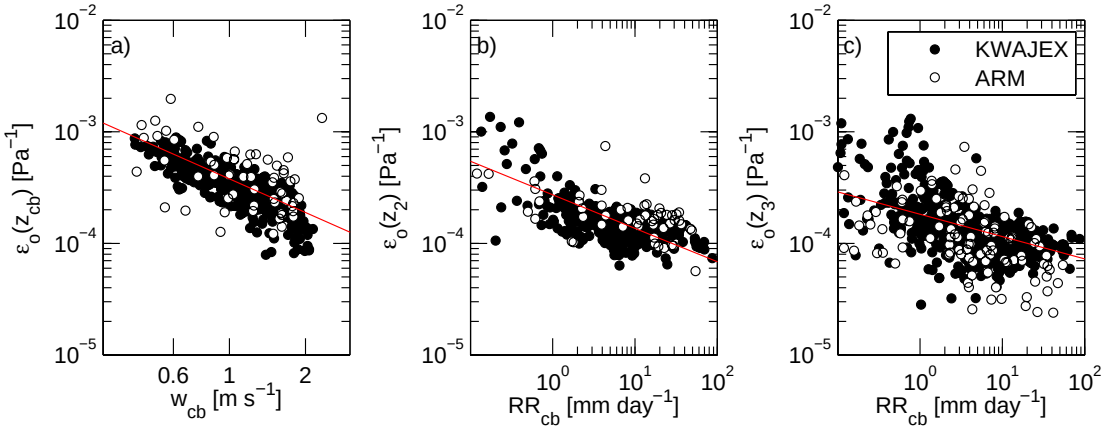

Fig. 7. Log-log scatter plots with regression line of **(a)** $\epsilon_0(z_{cb})$ versus w_{cb}, **(b)** $\epsilon_0(z_2)$ versus RR_{cb} and **(c)** $\epsilon_0(z_3)$ versus RR_{cb}. Full circles for KWAJEX, open circles for ARM. Regression lines in **(a)**, **(b)** and **(c)** are given by Eqs. (5), (7), and (8), respectively.

ACPD
11, 8385–8430, 2011

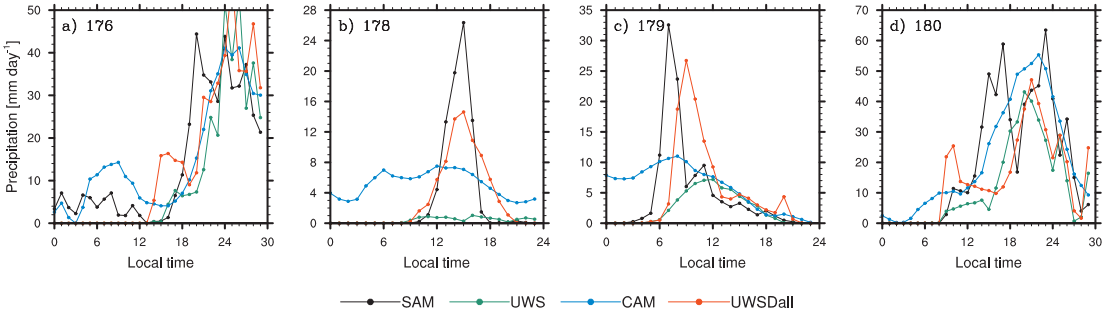

Fig. 8. Same as Fig. 5 but for SAM, UWS, CAM and UWSDall.

ACPD
11, 8385–8430, 2011

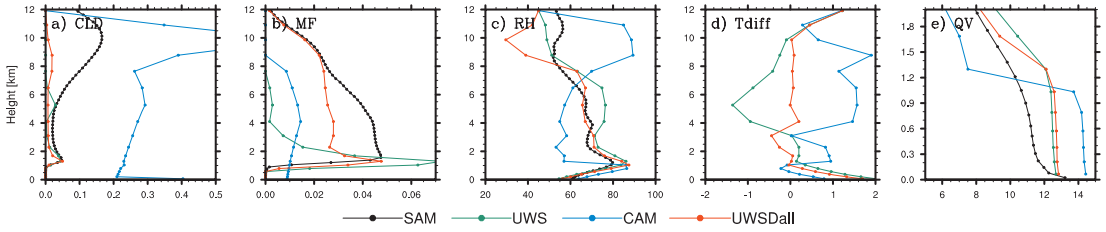

Fig. 9. Mean profiles of **(a)** cloud cover, **(b)** mass flux ($kg\,m^{-2}\,s^{-1}$), **(c)** relative humidity (%), and **(d)** temperature difference with respect to SAM (K) for ARM day 178. Lines as in Fig. 8. The profiles are averaged over the rain period, i.e., 10:00–18:00 LT. Panel **(e)** shows specific humidity ($g\,kg^{-1}$) at 15:00 LT on ARM day 178.

ACPD
11, 8385–8430, 2011

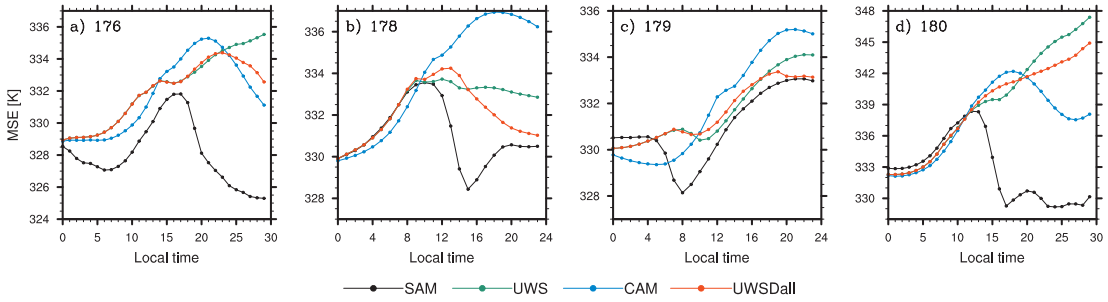

Fig. 10. Same as Fig. 8 but for MSE averaged over the lowest 1 km.

ACPD
11, 8385–8430, 2011

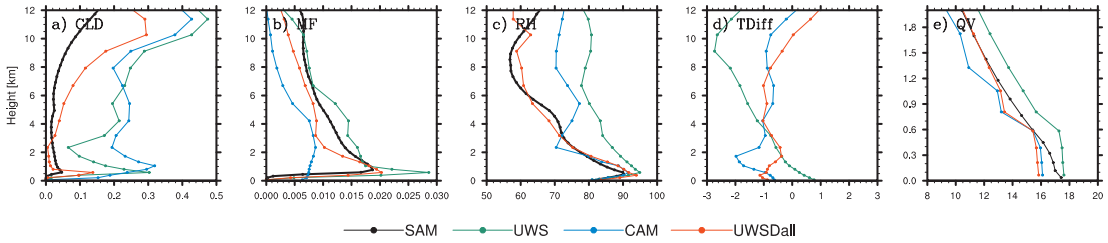

Fig. 11. Same as Fig. 9 but for KWAJEX. The profiles in **(a)**–**(d)** have been averaged over the full time period, while panel **(e)** displays a specific time under strong precipitation (hour 230 in the simulation).

ACPD
11, 8385–8430, 2011

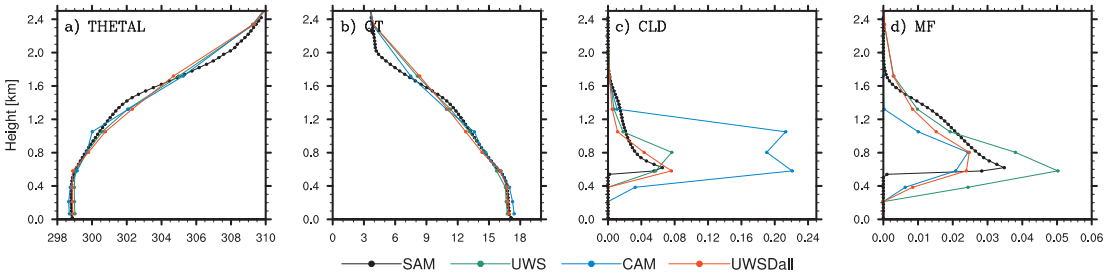

Fig. 12. Profiles of **(a)** liquid water potential temperature (K), **(b)** total specific humidity (g/kg), **(c)** cloud cover and **(d)** mass flux ($kg\,m^{-2}\,s^{-1}$) averaged over hours 3 to 6 of BOMEX, for the same simulations as in the previous figures.

ACPD
11, 8385–8430, 2011

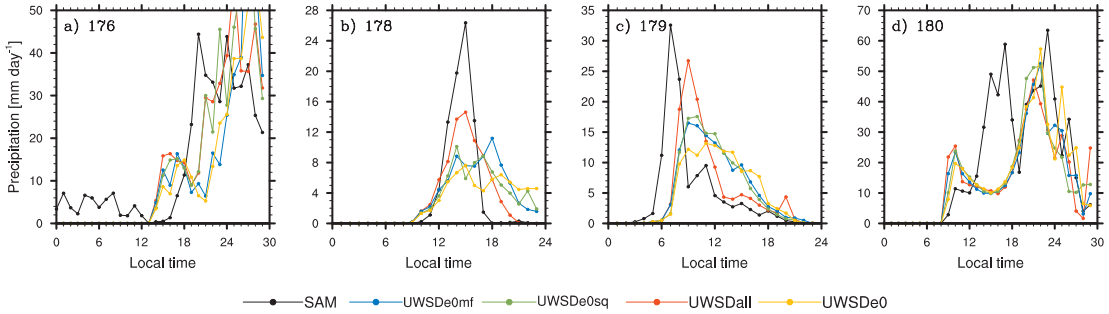

Fig. 13. Diurnal cycle of precipitation for ARM day **(a)** 176, **(b)** 178, **(c)** 179, and **(d)** 180. Black, blue, green, red and orange lines are for SAM, UWSDe0mf, UWSDe0sq, UWSDall and UWSDe0, respectively.

ACPD
11, 8385–8430, 2011

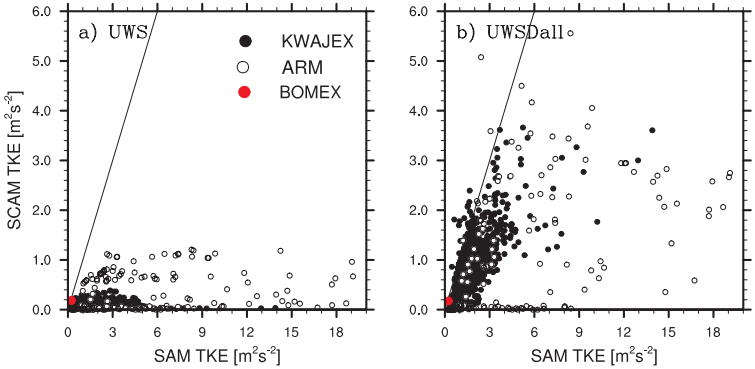

Fig. 14. Scatter plots of PBL averaged TKE in **(a)** UWS and **(b)** UWSDall versus SAM values. Black, white and red circles are for KWAJEX, ARM, and BOMEX, respectively. For KWAJEX and ARM, only points with precipitation are plotted. The BOMEX point corresponds to the mean over the simulation hours 3 to 6.

ACPD
11, 8385–8430, 2011